A more practical technique, which does not require the use of an optimal frequency domain filter, is to simply monitor the image estimate at the output of the linear filter $u(x, y)$, and terminate the process when a "visually optimal" result is achieved. In most situations, some subjective idea of the variance of the image is available. Results of this technique are shown in chapter 6.

Chapter 5

Novel Support-Finding Algorithm

This chapter presents a novel method of determining the support of the true image for situations in which the size of the true object is unavailable. It is inspired by the concept of cross-validation.

5.1 Introduction to Principle of Cross-validation

Cross-validation (CV) is a widely recognized technique in the field of data analysis. It is sometimes known as "leave-one-out" or predictive sample reuse. Historically, it has been used as a criterion for estimating the optimal regularization parameter in smoothing problems [63]. Recently, CV has been applied to image restoration applications. It has been shown to be a reliable estimator of regularization parameters [64], an effective stopping criterion [62], [61], and has been used for assessing the legitimacy of tentative constraints [65]. As discussed in chapter 2, it has also been proposed for blind image restoration [28].

The principle behind CV is straightforward. The data is divided into two sets: an estimation set and a validation set. The estimation set is used to obtain a model or estimate based on a particular parameter value or assumption. The validation set is then used to validate the performance of the model or estimate and thus the assumption. In this way, many competing parameter values or assumptions may be tested to find the most appropriate. The difficulty faced with dividing the data

into two sets is that it is necessary to use as much of the data as possible to obtain a reliable estimate, but it is also desirable to test the estimate on as much of the data that was excluded from the estimation process as possible. CV deals with this dilemma by allowing all the data to be used for both purposes.

The data is divided into M sets ($M > 1$). The assumption being tested is imposed on all the sets but one, and a validation error measure is computed for the omitted set. The process is repeated, selecting a different set each time, until all the sets have been exhausted. The validation error measures for each set are averaged to produce the validation error for the particular parameter value or assumption. In this way, all the data is used for both estimation and validation.

In image restoration applications, the data used for estimation and validation are the given blurred image pixels. The restored image estimate is validated by "reblurring" (convolving) it using the known PSF, and finding the energy of its deviation from the original blurred image pixels excluded from the estimation process. Unfortunately, the procedure becomes unreliable if the PSF model is inaccurate.

The following section presents a novel technique for objectively assessing the validity of a support size used for blind image restoration. The method is based on the principle of cross-validation.

5.2 CV Approach of Determining the Object Support Size

For situations in which the object support size is unknown, determining it by visual inspection often proves cumbersome and unreliable. Therefore, a method for assessing the optimal support size automatically and objectively is desirable. The proposed method is motivated by the CV methods used for non-blind image restoration.

Because in blind image restoration the PSF is unknown, it is impossible to validate the estimated image by reblurring it in the way discussed in the previous section. Therefore, another method of assessing a support is required. Instead of dividing the degraded image pixels into estimation and validation sets, the a priori information

can be divided into s ich sets. That is, we make use of the fact that the image is positive and of finite support. A support region S is assumed and the pixels outside the assumed support are randomly chosen to be in one of the M groups $\{\overline{S}_1, \ldots, \overline{S}_M\}$. All the pixels outside S, denoted by $\overline{S}$, are minimized except for those in group k. Specifically, the "restored" image $\hat{f}_k(x,y)$ is obtained by minimizing the following estimation error

$$\min_{\{u(x,y)\}} E(S) = \min_{\{u(x,y)\}} \sum_{(x,y)\in\overline{S}-\overline{S}_k} [\hat{f}(x,y) - L_B]^2$$

where $\hat{f}(x,y) = u(x,y) * g(x,y)$.

This estimation is validated by calculating the energy of $(\hat{f}(x,y) - L_B)$ for $(x,y) \in \overline{S}_k$, and the negative pixels within S. The nonnegativity of the image estimate is an objective measure of the authenticity of an assumed support. The validation error is given by

$$V(S) = \frac{1}{M}\sum_{k=1}^{M}\left[\sum_{(x,y)\in\overline{S}_k}[\hat{f}_k(x,y) - L_B]^2 + \sum_{(x,y)\in S}\hat{f}_k^2(x,y)\left[\frac{1-\mathrm{sgn}(\hat{f}_k(x,y)}{2}\right]\right]$$

The support region S^* which minimizes $V(S)$ is considered to be the optimal support for restoration. In practice, S may be chosen to be any shape, the parameters of which are varied to select the most appropriate support region. For the results presented in this thesis, the support is assumed to be rectangular with variable dimensions. The orientation is fixed.

5.3 Implementation Issues of the CV Approach

Since the full cross-validation procedure requires M "restorations" to assess a selected support, a simpler approach is suggested. The method requires much less computational time and power and does not substantially sacrifice the performance of the full procedure. The technique, commonly referred to as the *holdout* method, is implemented as a feasible alternative.

The validation error may be approximated by computing the error over only a single deleted set of pixels rather than all M sets. This way only a single restoration is required to assess a given support. The expression for the new validation error is

$$V_{HO}(S) = \frac{1}{\| \overline{S}_1 \|} \sum_{(x,y)\in\overline{S}_1} [\hat{f}_1(x,y) - L_B]^2 + \frac{1}{\| S \|} \sum_{(x,y)\in S} \hat{f}_1^2(x,y) \left[\frac{1 - \mathrm{sgn}(\hat{f}_1(x,y))}{2} \right]$$

where the deleted set is $\overline{S}_1$. Even though the procedure is equivalent to the holdout method, it is motivated by the CV approach, so it is considered to be a simplified form of CV.

In general, the CV criterion is nonlinear with respect to its parameters of interest and is difficult to minimize analytically. Therefore, numerical techniques must be employed to determine the minimizing support parameters. A search procedure is incorporated to find the minimum of the validation error function, which is in general multimodal. Fortunately, simulation results show that the validation error is smooth with respect to support parameters. Any local minima are dominated by large scale changes in the function. Therefore, the search procedure can initially consist of a selecting points on a widely spaced grid of possible support parameters. The grid is continually made finer to pinpoint the precise location of the minimum. The procedure in algorithmic form for rectangular support is provided in table 5.1.

Simulation results presented in chapter 6 demonstrate the reliable performance of the procedure.

Table 5.1: Summary of the support-finding algorithm

- Assume an equally spaced grid of support parameter values (L_x, L_y) from $(1,1)$ to $(N_{xg}-1, N_{yg}-1)$

  1) Select a rectangular support S with dimensions (L_x, L_y) from the grid. If all values in the grid have been selected before, either

  1. form a finer grid with the same number of elements centred about the minimum of the validation error found so far, and select a parameter set out of this.
  2. Go to step 6 if the exhausted grid contains successive elements.

  2) Randomly divide the pixels outside the selected support into M groups $\{\overline{S}_1, \ldots, \overline{S}_M\}$ of equally numbered elements.

  3) Based on S, "restore" the image by minimizing

$$\sum_{(x,y)\in\overline{S}-\overline{S}_1} [\hat{f}(x,y) - L_B]^2$$

  where $\hat{f}(x,y) = u(x,y) * g(x,y)$.

  4) Calculate the simplified validation error based on the minimizing parameters $u^*(x,y)$ of step 3.

$$V_{HO}(S) = \frac{1}{\| \overline{S}_1 \|} \sum_{(x,y)\in\overline{S}_1} [\hat{f}^*_1(x,y) - L_B]^2 + \frac{1}{\| S \|} \sum_{(x,y)\in S} \hat{f}^{*2}_1(x,y) \left[\frac{1 - \mathrm{sgn}(\hat{f}^*_1(x,y))}{2} \right]$$

  5) Go to step 1.

  6) Select the support parameters that minimize $V_{HO}(S)$ as the optimal support size for restoration.

Chapter 6

Simulation Results and Comparisons

The proposed blind deconvolution method for images is implemented using the steepest descent and conjugate gradient algorithms for optimization as summarized in tables 3.2 and 3.3, respectively. Simulations were conducted for the case of a uniformly black background ($L_B = 0$). For the results presented in this chapter, the following constraint was imposed on the parameters using the penalty method of section 4.1.3, with $\gamma = 1$, to avoid the trivial all-zero solution.

$$\sum_{x=1}^{N_{xu}} \sum_{y=1}^{N_{yu}} u(x,y) = 1$$

Simulation results of three existing methods[1] in the class of nonparametric finite support techniques are provided for comparison to assess the performance of the proposed algorithm.

The following acronyms are used to refer to the different techniques:

IBD Iterative blind deconvolution method

CG Conjugate gradient method

SA Simulated annealing algorithm

[1]Section 2.2 describes all three methods.

NAS-RIF Nonnegativity and support constraints recursive inverse filtering method proposed in this thesis

These methods are compared on the basis of their convergence properties, performance under ideal conditions, performance in the presence of noise, and performance when the size of the support is incorrect.

Simulations results are also shown for the proposed support-finding algorithm.

6.1 Convergence Properties

As mentioned in section 2.2, the convergence properties of the IBD method are unknown. The algorithm, at times, appears to converge to a solution, but then diverges on subsequent iterations. To avoid such problems, the IBD algorithm is implemented such that the best image estimate (in terms of the known conditions of nonnegativity and support), generated so far in the iterative process, is saved as the current image estimate. This is suggested in [18]. Because of the unpredictable behaviour of the method, the algorithm is not self-terminating; it is run for a pre-specified number of iterations. Simulation results on this algorithm reveal that although the method sometimes produces good results, it can become unstable. The convergence of the algorithm is highly dependent on the initial conditions, and parameter α shown in equation 2.1.

The CG method was proposed to alleviate the instability of the IBD method. It has definite termination conditions, and does not require fine tuning of specific parameters; however, the method is highly susceptible to becoming trapped in local minima of the nonconvex cost function. While the CG method showed global convergence for the test images shown in [24], the algorithm converged to local minima for the images presented in the simulations for this thesis.

The SA method attempts to compensate for the nonconvexity of its proposed cost function. However, it requires the "careful" reduction of the simulated annealing probability parameter p at each iteration. If p is reduced too quickly the algorithm can converge to a local minimum; if it is reduced too slowly, convergence to the global

minimum can be slow, in which case computational time is wasted. In general, the method is computationally demanding, even for reasonably small-sized images.

6.2 Comparison of the Performance of the Algorithms

Two related measures of performance will be used to help assess the quality of the restorations: the percentage mean square error (MSE) and signal-to-noise ratio improvement (SNRI). These quantities are defined below.

$$MSE(\hat{f}) \triangleq 100\frac{\sum_{\forall(x,y)}[a\hat{f}(x,y) - f(x,y)]^2}{\sum_{\forall(x,y)} f^2(x,y)}$$

$$SNRI \triangleq \frac{MSE(g)}{MSE(\hat{f})}$$

Because any scaled version of the image estimate is desired, a is chosen such that $MSE(\hat{f})$ is minimized. Specifically,

$$a = \frac{\sum_{\forall(x,y)} f(x,y)\hat{f}(x,y)}{\sum_{\forall(x,y)} \hat{f}^2(x,y)}$$

Even though the MSE is not a reliable estimator of the subjective quality of a restored image, it will be used to give some indication of the performance of the schemes.

Various combinations of images and blurs were tested in the simulations of the four algorithms. The most significant are presented. The three images tested in simulations are:

BIR image a synthetically generated binary text image of the words "BLIND IMAGE RESTORATION"

toy image a grey-scale image of a toy

UT image a synthetically generated binary image of the letters "UT"

Figure 6.1: Synthetic blurs used for simulations under ideal conditions

Each image was synthetically blurred using the linear degraded model of equation 1.3 with one of four types of PSFs, referred to by their dimensions. A brief description of each PSF is provided below. Figure 6.1 [2] displays the PSFs.

21 × 21 PSF a radially symmetric PSF, geometrically decreasing from the center by a factor of 0.8.

23 × 23 PSF a separable PSF generated from $\underline{v}\underline{v}^T$ where $\underline{v}$ is a column vector geometrically decreasing from the centre by a factor of 0.7.

51 × 51 PSF a nonsymmetric nonseparable PSF with a non-central peak

11 × 11 blur nonsymmetric nonseparable blur with negative values. Since PSF refers only to those blurs that are positive, "blur" will be used to describe this function instead of "PSF".

6.2.1 Quality of the Restoration in Ideal Conditions

This section presents the performance of the algorithms under ideal situations: noiseless conditions and correct support.

[2] Negative pixels are displayed as black.

Figures 6.3 to 6.10 show the results of the proposed NAS-RIF algorithm, the IBD method, and the SA method for noiseless conditions and assuming the availability of the exact object support. The CG method did not produce meaningful results for these images, and its results are, therefore, not shown.

Figures 6.3 to 6.6 correspond to results of restorations of the BIR image degraded by the 21 × 21 PSF for the NAS-RIF and IBD methods. The SA method is computationally too intensive to produce a restoration for a blurred image of this size. The results show the original and blurred images as well as the resulting restorations. Percentage mean square error as a function of iteration is also presented to show the rates of convergence of the methods.

The IBD method produced comparable results to the proposed NAS-RIF method for the 21 × 21 and 23 × 23 PSFs. The convergence rate for the IBD method was often much slower than the NAS-RIF method. For the 51 × 51 PSF and the 11 × 11 blur, the IBD method did not converge to an acceptable solution. Different initial conditions and α values were tested, but reasonable convergence was not obtained for any of them. In fact, the IBD method lost stability in all situations involving the 11 × 11 blur. Figure 6.6(f) shows the MSE for the first 200 iterations of the IBD method. The algorithm was terminated at this point because of instability.

Figures 6.7 to 6.9 show results of a grey-scale toy image with the 21 × 21 PSF, 23 × 23 PSF and 11 × 11 blur. The proposed NAS-RIF method produced a good estimate in all cases. The IBD method, however, failed to converge to a reasonable solution, and the SA method was too computationally time consuming.

Figure 6.10 shows the restorations of the UT image degraded by the 21 × 21 PSF for the NAS-RIF, IBD and SA methods. All techniques provided good results. The IBD method converged slower than the proposed NAS-RIF technique. The SA method converged in 40 cycles, which should not be confused with 40 iterations. Each cycle in the simulated annealing algorithm is composed of 50 scans on the image [25], which is effectively 200 iterations.

For many of the simulations presented, it is evident that the MSE plots for the NAS-RIF method appear spiked. The value of the MSE has a tendency to shoot up

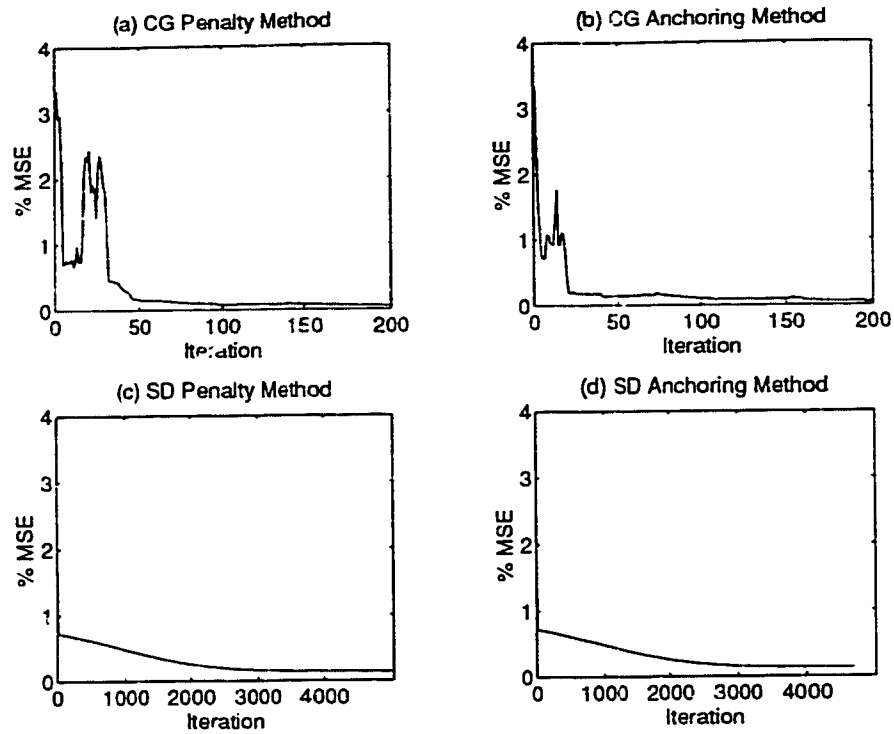

Figure 6.2: Mean square errors for NAS-RIF method using conjugate gradient and steepest descent minimization algorithms

unexpectedly as it appears to be settling. This is a result of the conjugate gradient minimization routine. The conjugate directions selected by the algorithm has a tendency to cause a rapid increase and decrease in the MSE. The steepest descent algorithm exhibits smooth behaviour. Figure 6.2 shows plots of the MSEs for the NAS-RIF method using the conjugate gradient and the steepest descent minimizations methods. The MSEs relate to the restoration of the toy image degraded by the 21×21 PSF. They are shown for two constraints on the parameters $u(x, y)$: the sum of the parameters $u(x, y)$ is equal to one, imposed using the penalty method with $\gamma = 1$, and the center tap of $u(x, y)$ is equal to one, imposed by anchoring it. Figures 6.2(a) and (b) correspond to the conjugate gradient algorithm and figures 6.2(c) and (d) correspond to the steepest descent method. Each minimization algorithm exhibits the same type of transient behaviour for both constraints.

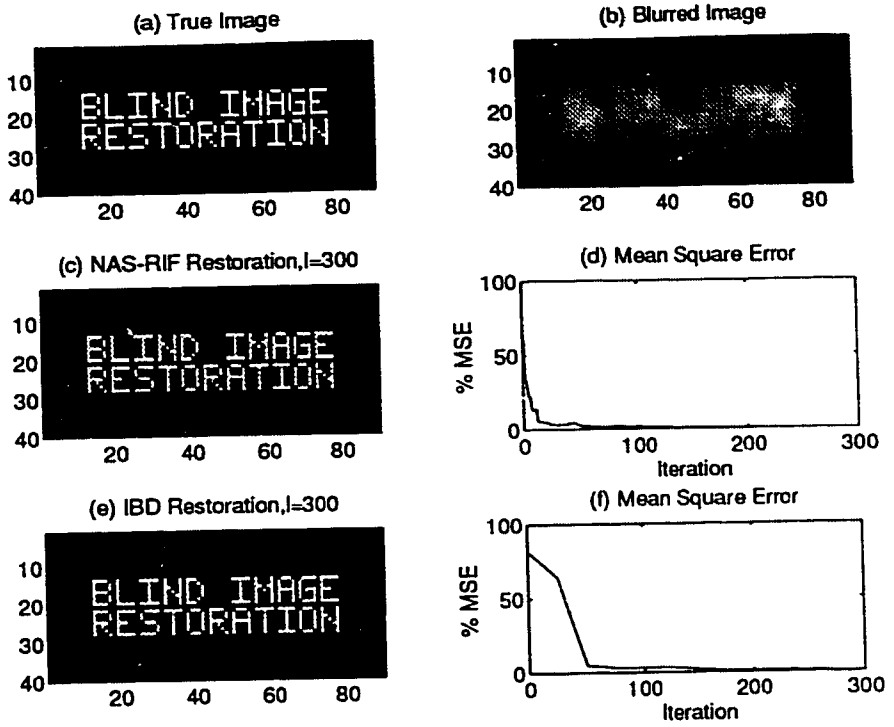

Figure 6.3: Results for the BIR image degraded by the 21 × 21 PSF under ideal conditions

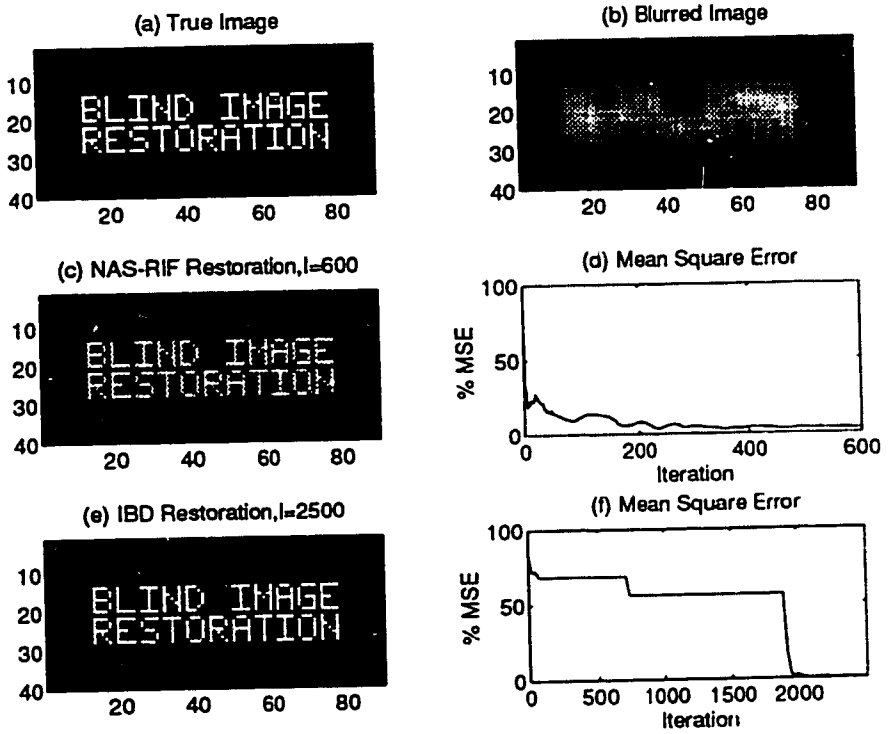

Figure 6.4: Results for the BIR image degraded by the 23 × 23 PSF under ideal conditions

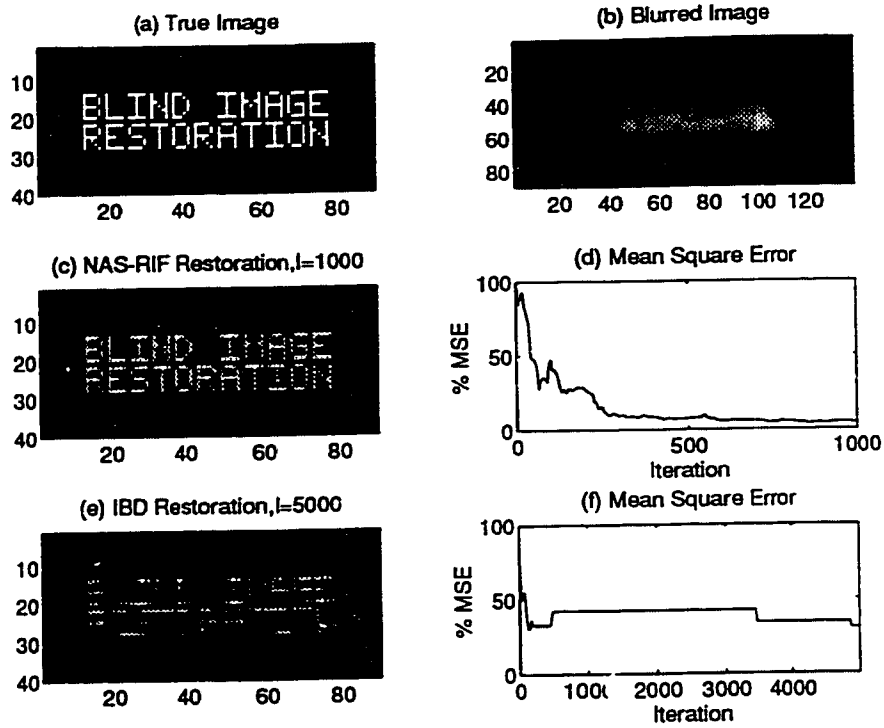

Figure 6.5: Results for the BIR image degraded by the 51 × 51 PSF under ideal conditions

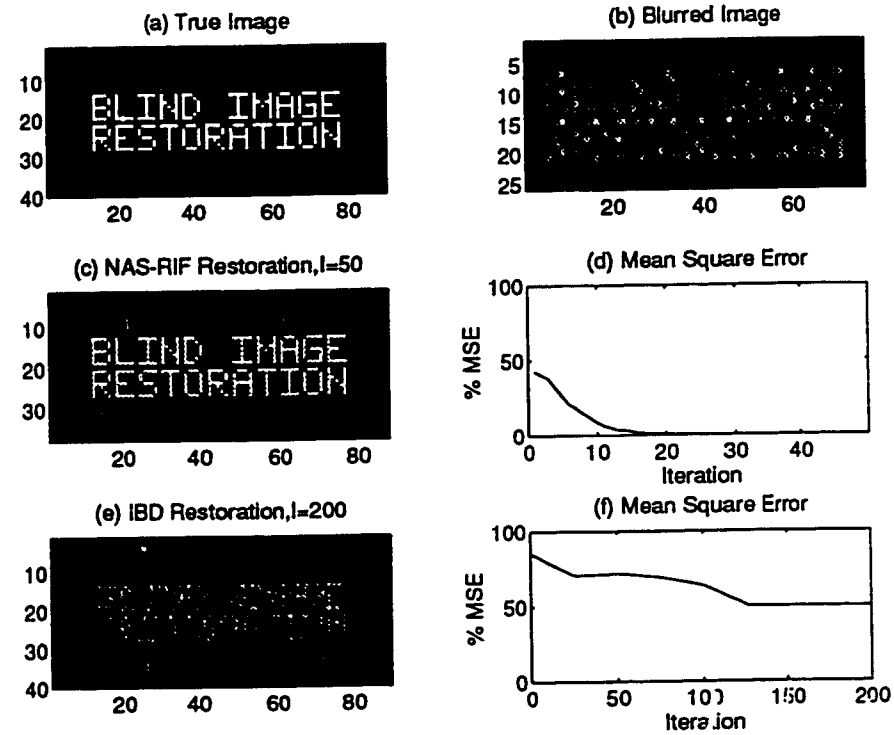

Figure 6.6: Results for the BIR image degraded by the 11 × 11 blur under ideal conditions

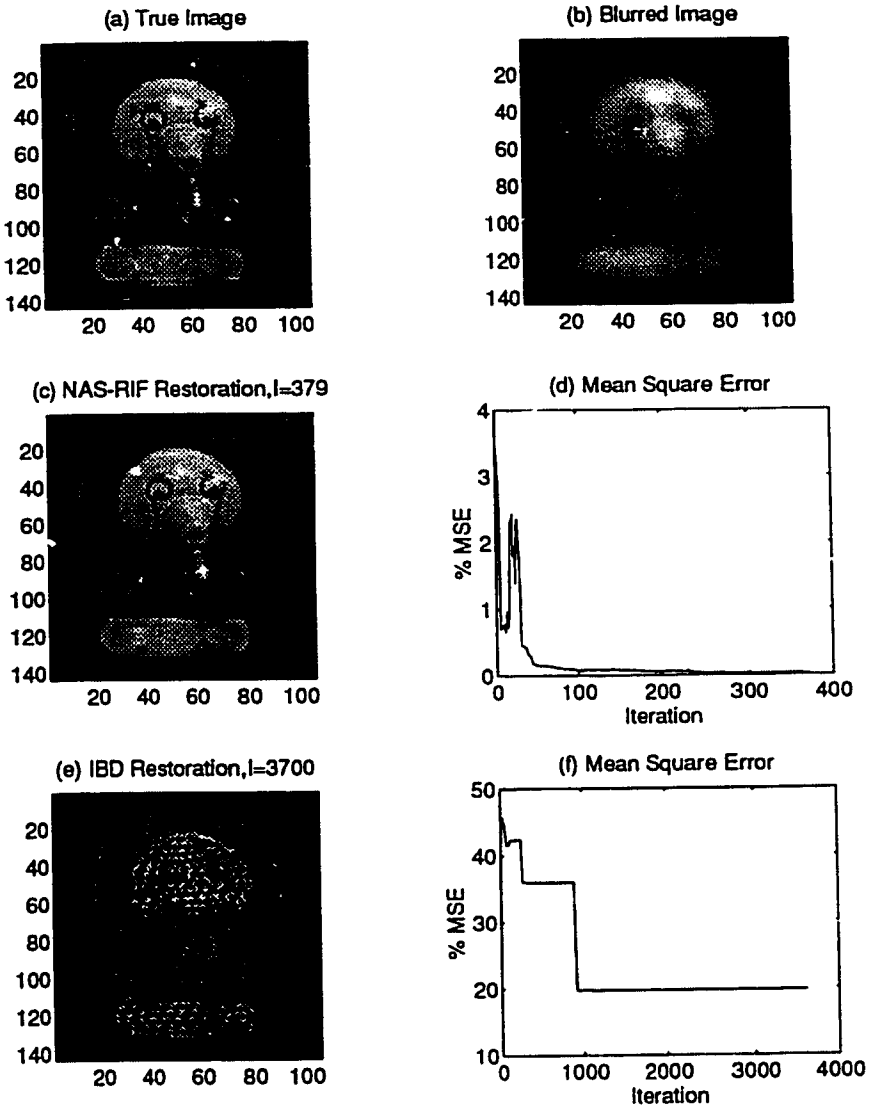

Figure 6.7: Results for the toy image degraded by the 21 × 21 PSF under ideal conditions

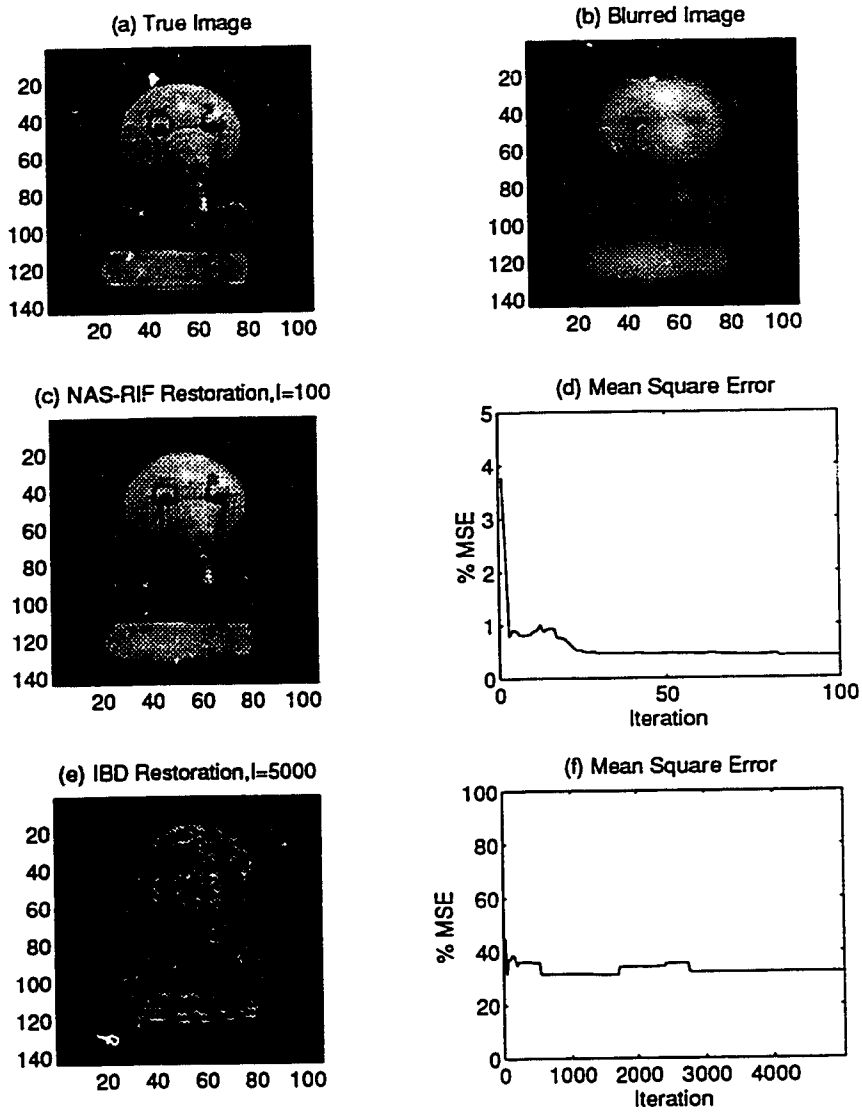

Figure 6.8: Results for the toy image degraded by the 23 × 23 PSF under ideal conditions

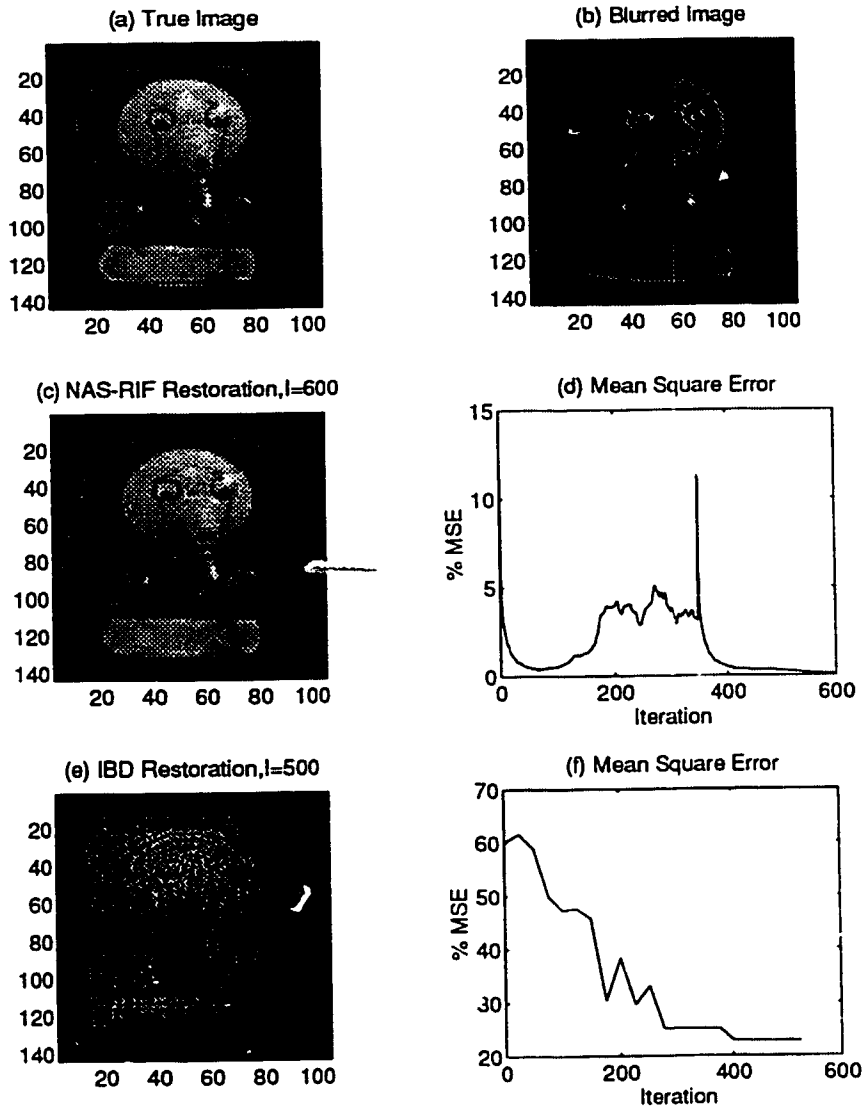

Figure 6.9: Results for the toy image degraded by the 11 × 11 blur under ideal conditions

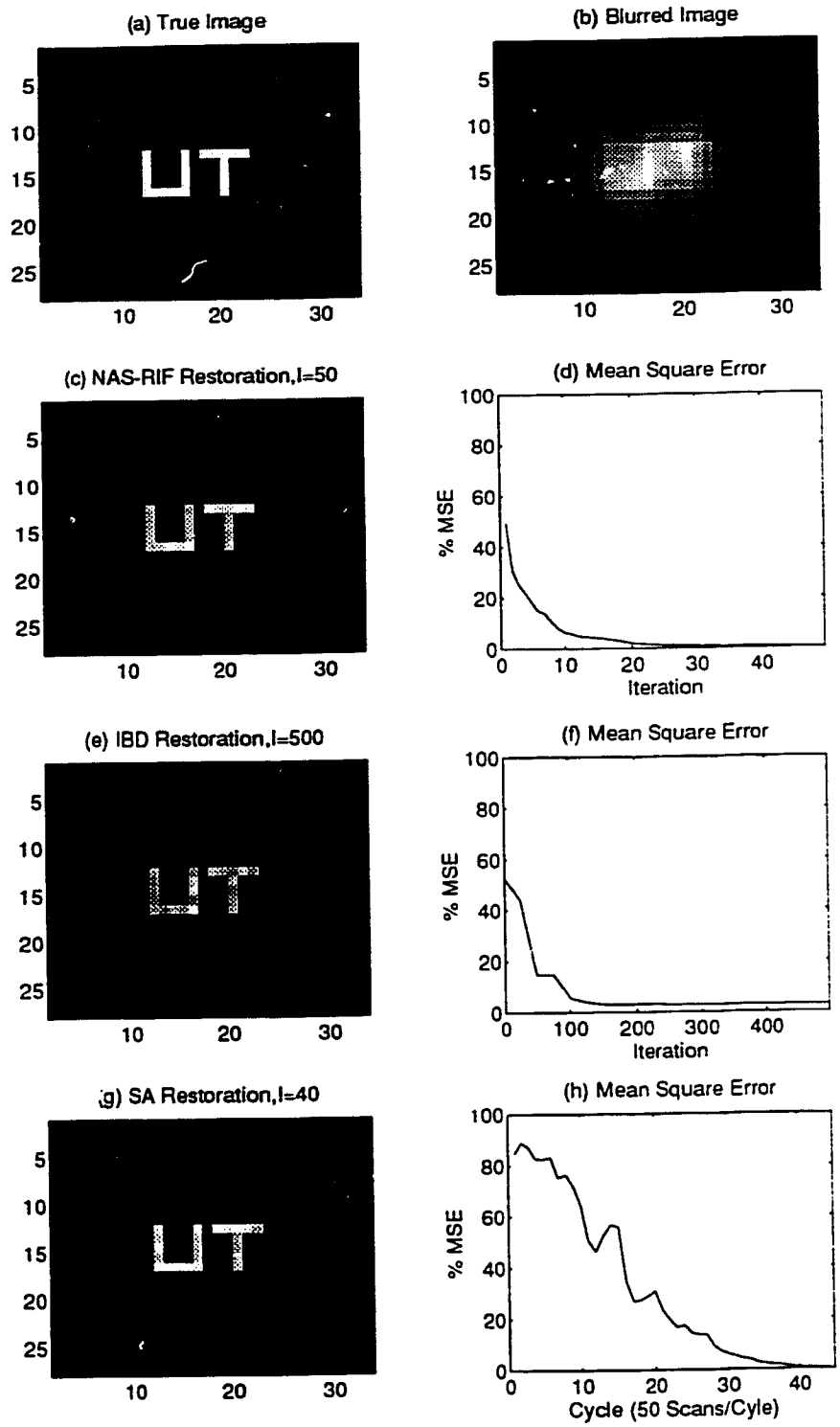

Figure 6.10: Results for the UT image degraded by the 23×23 PSF under ideal conditions

6.2.2 Robustness to Additive Noise

This section presents the results of the algorithms in the presence of additive white Gaussian noise. The blurred signal-to-noise ratio (BSNR) is used as a measure of the extent of degradation due to noise. It is defined as the ratio of the energy of the blurred signal to the energy of the noise.

$$BSNR \triangleq \frac{\sum_{\forall(x,y)} \tilde{g}^2(x,y)}{\sum_{\forall(x,y)} n^2(x,y)}$$

where $\tilde{g}(x,y) = f(x,y) * h(x,y)$ and $n(x,y)$ is the additive noise.

The IBD method proved to be more robust to noise than the other methods. The noise parameter α in the algorithm has the effect of suppressing noise amplification. Figure 6.11 shows results of the NAS-RIF and IBD methods for the restoration of the BIR image blurred by the 21 × 21 PSF at a BSNR of 50 dB. The best and worst estimates in terms of MSE are shown. The averages of 10 restorations using different noise realizations are also displayed. The best and averaged estimates are comparable for both methods. The worst estimate of the NAS-RIF method, shown in figure 6.11(c), is of poorer quality than that for the IBD method, shown in figure 6.11(d). The mean square errors are displayed in figures 6.11(g) and 6.11(h). The solid lines represent the MSEs for the best estimate case, and the dashed lines are the MSEs for the worst estimate case. The MSEs of figure 6.11(g) for the NAS-RIF method, both, initially began to converge to the desired solution. However, after subsequent iterations, the worst estimate case deviated and exhibited noise amplification at termination. Premature termination of the procedure would produce better results in the presence of noise.

Figure 6.11(h) shows the MSE plots for the IBD method. The MSEs both converge to an acceptable solution at termination, although the MSE for the worst estimate case takes longer. The IBD method is more effective at suppressing noise. However, experience shows that the noise parameter α must be carefully chosen for reliable restoration, even in the noiseless situation. The value of α is selected through trial and error.

Figure 6.12 shows the results of the NAS-RIF method for the toy image blurred by the 21 × 21 PSF at a BSNR of 50 dB. Very little noise amplification is evident in the best and worst estimates. Figure 6.12(d) shows the percentage mean square errors for the best (solid line), and worst (dashed line) estimates. The case of the best restoration, exhibits much faster convergence than that of the worst restoration. In addition, the sharp peaks in the MSE for the worst case, are not evident for the best estimate. Figure 6.13 shows the image estimate at different stages of the restoration procedure for 40 dB BSNR. As the iterations progress, the image initially gets clearer, then degrades because of noise amplification. Thus, premature termination is an effective method of regularizing the problem.

In general, the SA algorithm demonstrated a tolerance for noise above 40 dB. The optimal rate of decrease of the parameter p for global convergence had to found through trial and error. When acceptable convergence was achieved, its results were slightly better than that of the NAS-RIF algorithm without premature termination, and were poorer than the results of the IBD method and NAS-RIF method with premature termination.

6.2.3 Robustness to Incorrect Support Size

This section addresses the effect of incorrect support size on the restoration procedures. All restoration procedures demonstrated little tolerance for underestimated image support sizes. The IBD method was intolerant to overestimation of the image support sizes as well. The algorithm failed to converge properly for any of the simulations using incorrect support sizes. The simulation results of the proposed NAS-RIF method (using the BIR image and the 21 × 21 PSF) for overestimated and underestimated supports is shown in figure 6.14. The true image support is 15 × 65. The overestimated and underestimated supports are 17 × 67 and 13 × 63, respectively.

The proposed algorithm is highly robust to overestimation of the support size. Table 6.1 shows the SNRIs of the image estimates at differently assumed supports for the toy image degraded by the 21 × 21 PSF. In general, as the estimated support size gets close to the actual support value of 15 × 65, the SNRI increases. It should be

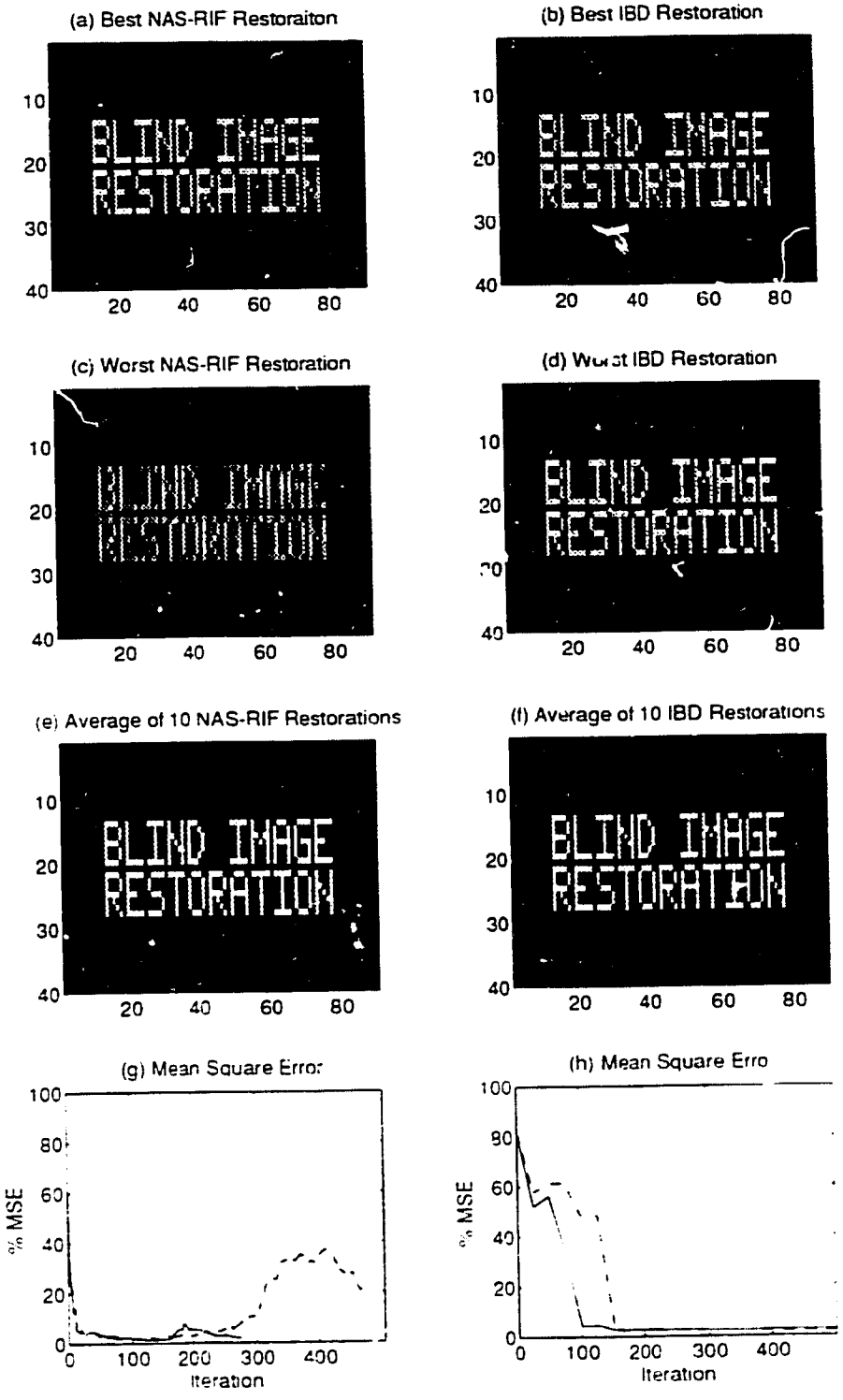

Figure 6.11: Results for the BIR image degraded by the 21×21 PSF at a BSNR of 50 dB

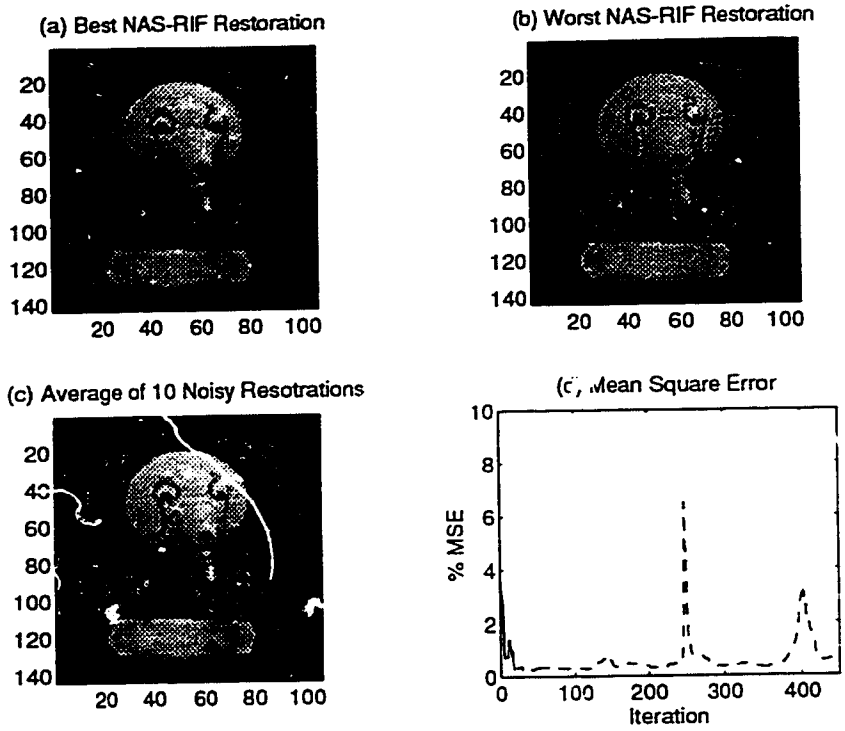

Figure 6.12: Results for the toy image degraded by the 21×21 PSF at a BSNR of 50 dB

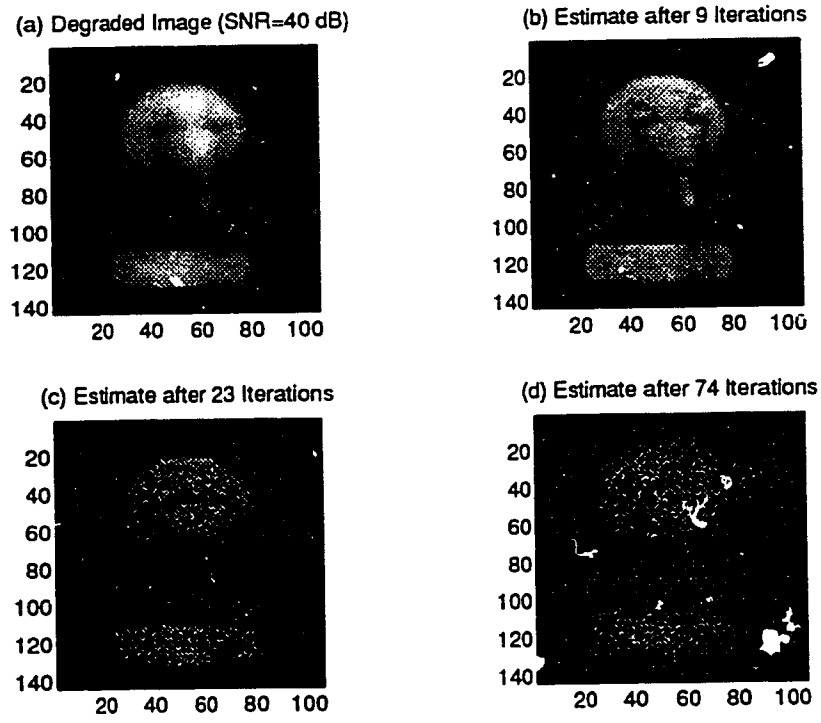

Figure 6.13: Progressive Image estimates for the BIR image degraded by the 21×21 PSF at a BSNR of 40 dB

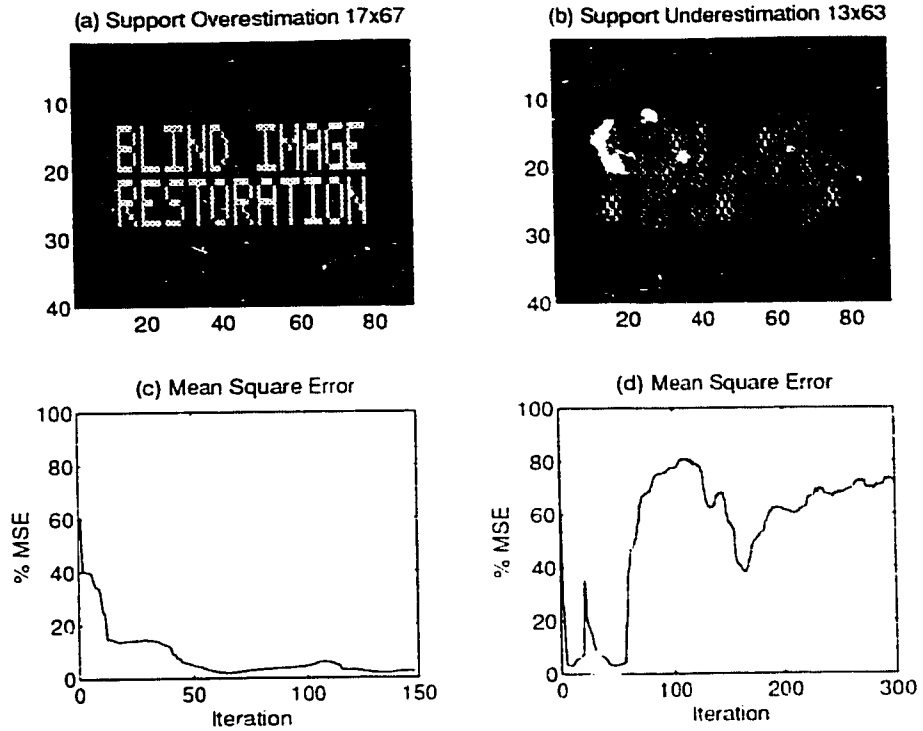

Figure 6.14: NAS-RIF algorithm results for inaccurate support sizes

noted that the maximum SNRI occurred for 121×83 which is a slight overestimation.

6.3 Performance of Support-Finding Algorithm

The proposed support-finding algorithm shows definite promise. Table 6.2 summarizes the results on the BIR image degraded by the 21×21 and 23×23 PSFs at 60 dB, and the 11×11 blur at 40 dB. The algorithm of table 5.1 was used with $M = 2$. The correct support size of the image is 15×65. In each simulation, the correct vertical dimension was estimated, and the horizontal dimension was slightly overestimated.

The support-finding algorithm was also applied on a degraded version of the toy image. The 21×21 PSF was used to blur the original image and noise was added to produce a BSNR of 60 dB. The algorithm of table 5.1 was used with $M = 2$. The search routine tested four grids of potential support sizes with successively finer points. Figure 6.15 shows the validation errors calculated at each of the points on the grids. The figure shows that the validation error is generally smooth, and doesn't possess any severe local extrema. The minimum validation error occurred at 120×81, which is close to the true value of 119×81.

Table 6.1: SNR Improvement as a function of estimated support size

estimated support	SNRI
127×89	15.8 dB
123×85	20.6 dB
121×83	22.2 dB
119×81	21.9 dB
117×79	0.6 dB
115×77	0.0 dB
111×73	0.0 dB

Table 6.2: Estimated support sizes from the support-finding algorithm

blur	Estimated Support
11 × 11 blur	15 × 69
21 × 21 blur	15 × 67
23 × 23 blur	15 × 75

Thus, the novel support-finding algorithm holds promise in blind image restoration.

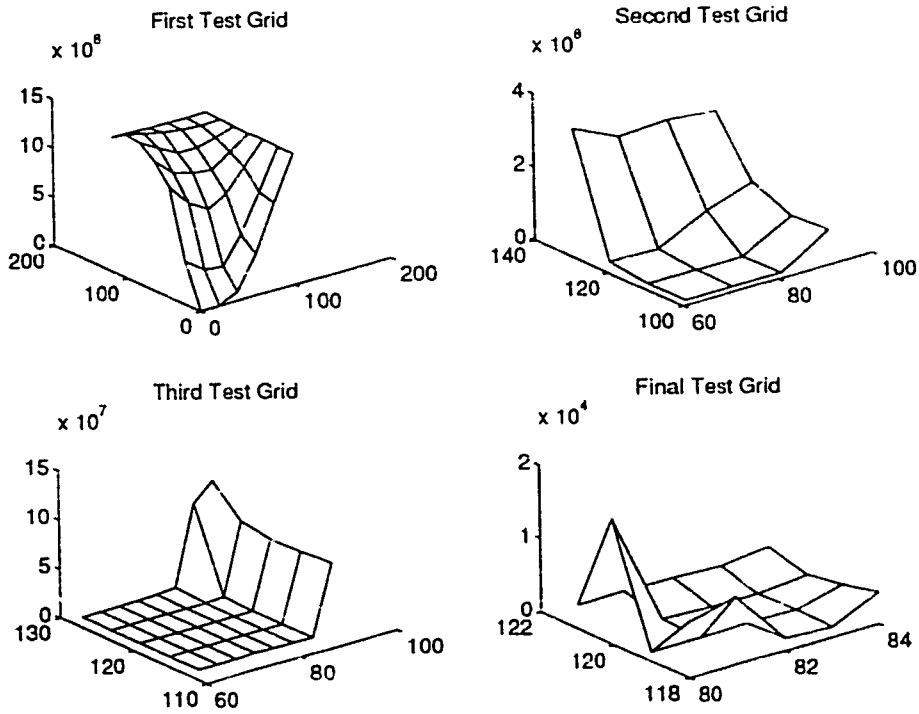

Figure 6.15: Validation errors for support-finding algorithm's search routine on the toy image degraded by the 21 × 21 PSF (BSNR = 60 dB)

Chapter 7

Conclusions and Further Research

7.1 Conclusions

A novel blind deconvolution scheme for the class of nonparametric finite support restoration methods is developed. It has clear advantages over existing techniques of its class because convergence to the feasible set of solutions is guaranteed. The convexity of the proposed cost function is proven analytically. The behaviour of the algorithm in the presence of finite extent equalizers and noise is examined, and performance improvement techniques are proposed to adjust for possible ill-effects.

For situations in which the support of the original image is unknown, a novel support-finding algorithm is presented. The algorithm is inspired by the principle of cross-validation. In CV, the given data is divided into two groups for estimation and validation. In the proposed method, the a priori knowledge about the true image is divided into these sets, yielding a method suitable for blind image restoration. In its computationally simpler form, the algorithm can be recognized to be the holdout method.

Simulation results of the proposed NAS-RIF algorithm are presented to demonstrate the potential of the technique for practical blind image restoration. Its performance is compared to that of existing methods of its class. The same assumptions about the true image are required for all algorithms. The existing IBD, SA, and CG methods require that the blur be nonnegative with known finite support. In contrast,

the proposed method requires that the blur only be invertible.

The proposed algorithm shows much better performance than existing techniques at high SNRs. Other methods demonstrate difficulties ranging from ill-convergence and instability to enormous computational requirements.

The IBD method works well for some of the binary images tested in this thesis. Results are comparable to the proposed NAS-RIF algorithm, but convergence of the IBD method is often slower. The IBD method is more effective in suppressing additive noise. Its major drawback is that it has difficulty converging to an acceptable solution for more complicated grey-scale images; instability often results. In addition, no specific termination conditions exist for the method, and the quality of restoration depends on the initial conditions and the noise parameter α.

The CG method has definite termination conditions and does not suffer from instabilities like the IBD method. However it often exhibits convergence to the local minima of its cost function. Experience shows that for images of size greater than 25×25, selection of initial conditions to achieve global convergence is nearly impossible.

The SA method produces comparable results to the NAS-RIF and IBD algorithms at high SNRs. Convergence to the global minimum depends on how the probability parameter p is reduced. If p is reduced too rapidly, then the method will converge to a local minimum. Convergence speed is, in general, extremely slow, so the method is limited to very small images and is, therefore, unsuitable for practical blind image restoration.

A drawback of the proposed method is that it is susceptible to excessive noise amplification at low SNRs. Early termination of the algorithm before such amplification is employed to produce acceptable results.

7.2 Further Research

The field of blind image restoration is still quite young and there exist many possible areas for further research. Those specifically related to the contributions made in this thesis are presented below:

- This thesis addresses the problem of blind image restoration on a single image frame. For many applications multiple frames exist in which the original images are highly correlated. This occurs in applications such as motion estimation, robot vision, and colour image processing. A modification of the algorithm to incorporate the correlation between frames can provide valuable information for the restoration procedure.

- The proposed scheme exhibits noise amplification at low SNRs. A reliable method of regularizing the problem (possibly by rolling off the equalizer transfer function) would be beneficial. To maintain convexity of the cost function, the parameters $u(x,y)$ must be constrained to lie in a convex set. Restricting $u(x,y)$ to be bandlimited represents a convex constraint. Thus, by imposing this restriction on the equalizer, noise amplification can be suppressed. The cut-off frequency that produces a visually appealing restoration needs to be investigated.

- The proposed technique uses a priori information about nonnegativity and support of the original image. Generalization of the algorithm for arbitrary constraints can provide insight into the type information that preserves convergence and uniqueness of the solution. The proposed method can be extended for use in a wider variety of applications.

- For applications in which the nonlinear properties of the imaging system are significant, a method of finding the parameters of the nonlinearity in conjunction with restoring the image can benefit many imaging facilities.

Appendix A

Proof of Convexity of Cost Function

A.1 Proof of Convexity of the Nonnegativity Constraint Cost Function

The following analysis proves that the following function, which corresponds to the nonnegativity constraint on the image estimate, is convex:

$$J_1 = \sum_{(x,y)\in D_{sup}} \hat{f}^2(x,y)\left[\frac{1-\mathrm{sgn}(\hat{f}(x,y))}{2}\right]$$

It is common in convex analysis to approximate a given function J by a sequence of more "regular" functions J_r. To select a sequence of functions J_r, regularization based on the convolution operation may be performed [44]. A "kernel function" $K : \mathbf{R} \rightarrow \mathbf{R}^+$, which is continuous, vanishes outside some compact interval, and is constrained such that $\int_{\mathbf{R}} K(y)dy = 1$ is chosen. The function $K_r(y)$ for positive integer r is defined as:

$$K_r(y) := K(ry) \text{ for } y \in \mathbf{R}$$

for which $J(x)$ may be approximated as:

$$J_r(x) := J(x) * K_r(x) = \int_{\mathbf{R}} J(x-y)K_r(y)dy$$

for $x, y \in \mathbf{R}$, where r is known as the regularization constant. The smoothness properties of J_r depend on those of K. For instance, if $K \in C^\infty$, a C^∞ regularization is obtained.

If such a sequence for J_1 can be used, then the following theorem may be used to prove convexity.

Theorem A.1 *Let the convex functions $J_r : \mathbf{R}^N \to \mathbf{R}$ converge pointwise for $r \to \infty$ to $J : \mathbf{R}^N \to \mathbf{R}$. Then J is convex and for each compact set S, the convergence of J_r to J is uniform on S.*

A commonly used kernel is introduced below:

$$K(y) := \begin{cases} ce^{\frac{1}{y^2-1}} & \text{for } |y| < 1 \\ 0 & \text{for } |y| \geq 1 \end{cases}$$

where $c > 0$ is chosen so that $\int_{\mathbf{R}} K(y)dy = 1$.

For $J(f) = f^2\left[\frac{1-\mathrm{sgn}(f)}{2}\right]$ where $\mathrm{sgn}(\cdot)$ is defined in equation 3.4, a sequence $J_r(f)$ may be formed as shown below.

$$\begin{aligned} J_r(f) &= J(f) * K_r(f) \\ &= \int_{-1/r}^{1/r} (f-y)^2 \left[\frac{1-\mathrm{sgn}(f-y)}{2}\right] ce^{\frac{1}{r^2y^2-1}} dy \\ &= \begin{cases} c\int_{-1/r}^{1/r} (f-y)^2 e^{\frac{1}{r^2y^2-1}} dy & \text{for } f \leq -1/r \\ c\int_{f}^{1/r} (f-y)^2 e^{\frac{1}{r^2y^2-1}} dy & \text{for } -1/r < f < 1/r \\ 0 & \text{for } f \geq 1/r \end{cases} \end{aligned}$$

Taking the second derivative of $J_r(f)$ with respect to f gives

$$\frac{\partial^2 J_r(f)}{\partial f^2} = \begin{cases} 2c\int_{-1/r}^{1/r} e^{\frac{1}{r^2y^2-1}}dy & \text{for } f \le -1/r \\ 2c\int_{f}^{1/r} e^{\frac{1}{r^2y^2-1}}dy & \text{for } -1/r < f < -1/r \\ 0 & \text{for } f \ge 1/r \end{cases}$$

$$= \begin{cases} 2 & \text{for } f \le -1/r \\ 2\dfrac{\int_{f}^{1/r} e^{\frac{1}{r^2y^2-1}}dy}{\int_{-1/r}^{1/r} e^{\frac{1}{r^2y^2-1}}dy} & \text{for } -1/r < f < 1/r \\ 0 & \text{for } f \ge 1/r \end{cases} \qquad (A.1)$$

Thus defining a sequence of functions $J_{1r} \subset C^\infty$ for $r \in \mathbf{Z}$ such that

$$J_{1r} := \begin{cases} \sum_{(x,y)\in D_{sup}} c\int_{-1/r}^{1/r}(\hat{f}(x,y)-\xi_{xy})^2 e^{\frac{1}{r^2\xi_{xy}^2-1}}d\xi_{xy} & \text{for } \hat{f}(x,y) \le -1/r \\ \sum_{(x,y)\in D_{sup}} c\int_{\hat{f}(x,y)}^{1/r}(\hat{f}(x,y)-\xi_{xy})^2 e^{\frac{1}{r^2\xi_{xy}^2-1}}d\xi_{xy} & \text{for } -1/r < \hat{f}(x,y) < -1/r \\ 0 & \text{for } \hat{f}(x,y) \ge 1/r \end{cases}$$

where $\xi_{xy} \in \mathbf{R}$. The Hessian of J_{1r} with respect to $\{u(1,1),\ldots,u(N_{xu},N_{yu})\}$ can be calculated using equation A.1 to be

$$J_{1r} = \sum_{(x,y)\in D_{sup}} A_r(x,y)\underline{G}(x,y)$$

where

$$\underline{G}(x,y) = \begin{bmatrix} g^2(x,y) & \cdots & g(x,y)g(x-N_{xu},y-N_{yu}) \\ \vdots & & \vdots \\ g(x-N_{xu},y-N_{yu})g(x,y) & \cdots & g^2(x-N_{xu},y-N_{yu}) \end{bmatrix}$$

and

$$A_r(x,y) := \begin{cases} 2 & \text{for } \hat{f}(x,y) \le 1/r \\ 2\int_{\hat{f}(x,y)}^{1/r} e^{\frac{1}{r^2y^2-1}}dy & \text{for } -1/r < \hat{f}(x,y) < 1/r \\ 0 & \text{for } \hat{f}(x,y) \ge 1/r \end{cases} \qquad (A.2)$$

where $\underline{G}(x,y)$ is lexicographically ordered. Because $A_r(x,y) \ge 0$ for all (x,y),

$\nabla^2 J_{1r}$ is in the form of a sum of nonnegatively scaled positive semi-definite matrices, which is also positive semi-definite. Thus, from theorem 3.1, J_{1r} is convex for $r \in Z$ which implies that J_1 is convex through theorem A.1.

A.2 Proof of Convexity of Support Constraint Cost Function

The following analysis proves that the following function, which corresponds to the support constraint on the image estimate, is convex:

$$J_2 = \sum_{(x,y)\in\overline{D_{sup}}} [\hat{f}(x,y) - L_B]^2$$

The Hessian of J_2 with respect to parameters $\{u(1,1),\ldots,u(N_{xu},N_{yu})\}$ is easily calculated.

$$\frac{\partial J_2}{\partial u(x_1,y_1)} = 2 \sum_{(x,y)\in\overline{D_{sup}}} \hat{f}(x,y) g(x-x_1+1, y-y_1+1)$$

and

$$\frac{\partial^2 J_2}{\partial u(x_1,y_1)\partial u(x_2,y_2)} = 2 \sum_{(x,y)\in\overline{D_{sup}}} g(x-x_1+1, y-y_1+1) g(x-x_2+1, y-y_2+1)$$

Therefore,

$$\nabla^2 J_2 = 2 \sum_{(x,y)\in\overline{D_{sup}}} \begin{bmatrix} g^2(x,y) & \cdots & g(x,y)g(x-N_{xu}+1, y-N_{yu}+1) \\ \vdots & & \vdots \\ g(x-N_{xu}+1, y-N_{yu}+1)g(x,y) & \cdots & g^2(x-N_{xu}+1, y-N_{yu}+1) \end{bmatrix} \tag{A.3}$$

Because $\nabla^2 J_2$ is in the form of a covariance matrix which is known to be positive semi-definite, J_2 is convex from theorem 3.1. Therefore, J is convex with respect to its parameters $\{u(1,1),\ldots,u(N_{xu},N_{yu})\}$.

Since J_1 and J_2 are both convex, it follows from theorem 3.2 that J is also convex.

Appendix B

Analysis of the Effect of Truncation of Equalizer on Global Minimum of Cost Function

The following analysis shows that if the two-dimensional FIR inverse $u(x,y)$ filter is made sufficiently large in extent, the global minimum of the cost function occurs "close" to the global minimum in the case for which $u(x,y)$ is infinite in extent. Noiseless conditions are assumed.

The true inverse of the blur $u^*(x,y)$ is assumed to be absolutely summable, that is

$$\sum_{x=-\infty}^{\infty}\sum_{y=-\infty}^{\infty}|u^*(x,y)| = S_u < \infty \tag{B.1}$$

Without loss of generality, the two-dimensional inverse filter is parametrized using $(2N_x+1)\times(2N_y+1)$ taps. The constant ε is chosen such that $\varepsilon > 0$ and

$$\sum_{|x|\geq N_x+1}\sum_{|y|\geq N_y+1}|u^*(x,y)| \leq \varepsilon \sum_{x=-\infty}^{\infty}\sum_{y=-\infty}^{\infty}|u^*(x,y)| \tag{B.2}$$

One can always choose a pair (N_x, N_y) such that

$$u^{(N_x,N_y)}(x,y) = \begin{cases} u^*(x,y) & \text{for } |x| \leq N_x \text{ and } |y| \leq N_y \\ 0 & \text{for } |x| > N_x \text{ or } |y| > N_y \end{cases} \tag{B.3}$$

Therefore, $u^{(N_x,N_y)}(x,y)$ is of finite extent. The proposed cost function becomes:

$$J(u^{(N_x,N_y)}) = \sum_{(x,y)\in D_{neg}(u^{(N_x,N_y)})} [u^{(N_x,N_y)}(x,y) * g(x,y)]^2 + \sum_{(x,y)\in \overline{D_{sup}}} [u^{(N_x,N_y)}(x,y) * g(x,y) - L_B]^2 \tag{B.4}$$

where $D_{neg}(u^{(N_x,N_y)})$ is the set of pixels of $[u^{(N_x,N_y)}(x,y) * g(x,y)]$ that are negative within D_{sup}, $\overline{D_{sup}}$ is the set of pixels outside the region of support of the true image, and $*$ represents two-dimensional discrete linear convolution. For simplicity, D_{neg} will be used instead of $D_{neg}(u^{(N_x,N_y)})$, but the dependence of D_{neg} on $u^{(N_x,N_y)}$ should be noted.

Substituting $[u^*(x,y) + u^{(N_x,N_y)}(x,y) - u^*(x,y)]$ for $u^{(N_x,N_y)}(x,y)$ in equation B.4 and expanding gives:

$$\begin{aligned} J(u^{(N_x,N_y)}) = & \\ & \sum_{(x,y)\in D_{neg}} [u^*(x,y) * g(x,y)]^2 + \sum_{(x,y)\in \overline{D_{sup}}} [u^*(x,y) * g(x,y) - L_B]^2 \\ + & \sum_{(x,y)\in D_{neg}} [(u^{(N_x,N_y)}(x,y) - u^*(x,y)) * g(x,y)]^2 \\ + & \sum_{(x,y)\in \overline{D_{sup}}} [(u^{(N_x,N_y)}(x,y) - u^*(x,y)) * g(x,y) - L_B]^2 \\ + & 2 \sum_{(x,y)\in D_{neg}} [u^*(x,y) * g(x,y)][(u^{(N_x,N_y)}(x,y) - u^*(x,y)) * g(x,y)] \\ + & 2 \sum_{(x,y)\in \overline{D_{sup}}} [u^*(x,y) * g(x,y) - L_B][(u^{(N_x,N_y)}(x,y) - u^*(x,y)) * g(x,y)] \end{aligned} \tag{B.5}$$

Letting

$$\begin{aligned} f^{(N_x,N_y)}(x,y) &:= u^{(N_x,N_y)} * g(x,y) \text{ and} \\ f^*(x,y) &:= u^*(x,y) * g(x,y) \end{aligned}$$

and using the relation of equation B.3, equation B.5 becomes,

$$
\begin{aligned}
&J(u^{(N_x,N_y)}) = \\
&\quad \sum_{(x,y)\in D_{neg}} [f^*(x,y)]^2 + \sum_{(x,y)\in \overline{D_{sup}}} [f^*(x,y) - L_B]^2 \\
&+ \sum_{(x,y)\in D_{neg}} [\sum_{|x'|\geq N_x+1} \sum_{|y'|\geq N_y+1} u^*(x',y')g(x-x',y-y')]^2 \\
&+ \sum_{(x,y)\in \overline{D_{sup}}} [\sum_{|x'|\geq N_x+1} \sum_{|y'|\geq N_y+1} u^*(x',y')g(x-x',y-y') - L_B]^2 \\
&+ 2 \sum_{(x,y)\in D_{neg}} f^*(x,y)[\sum_{|x'|\geq N_x+1} \sum_{|y'|\geq N_y+1} u^*(x',y')g(x-x',y-y')] \\
&+ 2 \sum_{(x,y)\in \overline{D_{sup}}} [f^*(x,y) - L_B][\sum_{|x'|\geq N_x+1} \sum_{|y'|\geq N_y+1} u^*(x',y')g(x-x',y-y')] \\
\leq &\quad \sum_{(x,y)\in D_{neg}} [f^*(x,y)]^2 + \sum_{(x,y)\in \overline{D_{sup}}} [f^*(x,y) - L_B]^2 \\
&+ G_{max}^2 \sum_{(x,y)\in D_{neg}} [\sum_{|x'|\geq N_x+1} \sum_{|y'|\geq N_y+1} |u^*(x',y')|]^2 \\
&+ G_{max}^2 \sum_{(x,y)\in \overline{D_{sup}}} [\sum_{|x'|\geq N_x+1} \sum_{|y'|\geq N_y+1} |u^*(x',y')|]^2 \\
&+ 2G_{max} \sum_{(x,y)\in D_{neg}} f^*(x,y)[\sum_{|x'|\geq N_x+1} \sum_{|y'|\geq N_y+1} |u^*(x',y')|] \\
&+ 2G_{max} \sum_{(x,y)\in \overline{D_{sup}}} [f^*(x,y) - L_B][\sum_{|x'|\geq N_x+1} \sum_{|y'|\geq N_y+1} |u^*(x',y')|]
\end{aligned}
$$

where the following property is used

$$
\begin{aligned}
&\sum_{|x'|\geq N_x+1} \sum_{|y'|\geq N_y+1} u^*(x',y')g(x-x',y-y') \\
&\quad \leq \sum_{|x'|\geq N_x+1} \sum_{|y'|\geq N_y+1} |u^*(x',y')||g(x-x',y-y')| \\
&\quad \leq G_{max} \sum_{|x'|\geq N_x+1} \sum_{|y'|\geq N_y+1} |u^*(x',y')|
\end{aligned}
$$

The constant G_{max} represents the maximum value of $|g(x,y)|$ for all (x,y).

Using equation B.1 and the inequality of B.2,

$$
\begin{aligned}
&J(u^{(N_x,N_y)}) \leq \\
&\quad \sum_{(x,y)\in D_{neg}} [f^*(x,y)]^2 + \sum_{(x,y)\in \overline{D_{sup}}} [f^*(x,y) - L_B]^2
\end{aligned}
$$

$$+ \quad \varepsilon^2 G_{max}^2 S_u^2 [\| D_{neg} \| + \| \overline{D_{sup}} \|]$$
$$+ \quad 2\varepsilon G_{max} S_u [\sum_{(x,y)\in D_{neg}} f^*(x,y) + \sum_{(x,y)\in \overline{D_{sup}}} (f^*(x,y) - L_B)]$$

where $\| \cdot \|$ represents the number of elements in the given set.

Using the fact that

$$f^*(x,y) = f^{(N_x,N_y)}(x,y) + \sum_{|x'|\geq N_x+1} \sum_{|y'|\geq N_y+1} u(x',y') g(x-x', y-y')$$

and that

$$\sum_{|x'|\geq N_x+1} \sum_{|y'|\geq N_y+1} u(x',y') g(x-x', y-y') \leq \varepsilon G_{max} S_u$$

the following relationship is derived

$$f^{(N_x,N_y)}(x,y) \geq f^*(x,y) - \varepsilon G_{max} S_u \tag{B.6}$$

Therefore,

$$\begin{aligned} D_{neg} &= \{(x,y) : f^{(N_x,N_y)}(x,y) < 0\} \cap D_{sup} \\ &= \{(x,y) : f^*(x,y) < \varepsilon G_{max} S_u\} \cap D_{sup} \end{aligned} \tag{B.7}$$

from equation B.6.

$J(u^{(N_x,N_y)})$ can be further bounded with the aid of B.7, and the fact that $f^*(x,y) \geq 0$ (since $f^*(x,y)$ is the true image in the noiseless situation).

$$\begin{aligned} J(u^{(N_x,N_y)}) \leq & \\ & \varepsilon^2 G_{max}^2 S_u^2 \| D_{neg} \| \\ + & \sum_{(x,y)\in \overline{D_{sup}}} [f^*(x,y) - L_B]^2 \\ + & \varepsilon^2 G_{max}^2 S_u^2 [\| D_{neg} \| + \| \overline{D_{sup}} \|] \\ + & 2\varepsilon G_{max} S_u [\varepsilon G_{max} S_u \| D_{neg} \| + \sum_{(x,y)\in \overline{D_{sup}}} (f^*(x,y) - L_B)] \end{aligned} \tag{B.8}$$

$$\sum_{(x,y)\in D^*_{neg}} [f^*(x,y)]^2 \tag{B.9}$$

where $D^*_{neg} = \{(x,y) : f^*(x,y) < 0\} \cap D_{sup}$. The final term of B.8, which is equal to zero, has been added.

Letting J^* represent the minimum cost in the infinite parameter case, we see that the second and final terms of inequality B.8 is equal to J^*. Therefore, we find that

$$J(u^{(N_x,N_y)}) \leq J^* + \varepsilon^2 G^2_{max} S^2_u [4 \parallel D_{neg} \parallel + \parallel \overline{D_{sup}} \parallel] + \varepsilon G_{max} S_u [\sum_{(x,y)\in\overline{D_{sup}}} (f^*(x,y) - L_B)]$$

Because $f^*(x,y)$ is the true image, $f^*(x,y) = L_B$ for $(x,y) \in \overline{D_{sup}}$ and the bound becomes

$$J(u^{(N_x,N_y)}) \leq J^* + \varepsilon^2 G^2_{max} S^2_u [4 \parallel D_{neg} \parallel + \parallel \overline{D_{sup}} \parallel] \tag{B.10}$$

Since the inverse filter parameters $u(x,y)$ are continuous with respect to J, it follows that if $J^* \approx J(u^{(N_x,N_y)})$, then the global minimum for the finite parameter case is "near" $u^*(x,y)$.

Therefore, by making the number of two-dimensional equalizer taps sufficiently large, ε can be made arbitrarily small, resulting in the image estimate close to the true image.

Appendix C

Analysis of the Effect of Noise on the Proposed Algorithm

C.1 Effect of Noise on the Global Minimum

Because the proposed cost function J is nonlinear, an exact relationship between the global minima in the presence and absence of noise is difficult to characterize. This section derives the value of the cost function at the true inverse blur parameter setting for noisy conditions and assuming infinite extent equalizers are available. This value gives an indication of the bias introduced in the restored image. The proposed cost function may be represented as:

$$\begin{aligned} J &= \sum_{(x,y)\in D_{sup}} \hat{f}^2(x,y)\mathrm{cl}(\hat{f}(x,y)) \\ &\quad + \sum_{(x,y)\in \overline{D_{sup}}} (\hat{f}(x,y) - L_B)^2 \end{aligned} \tag{C.1}$$

The image estimate $\hat{f}(x,y)$ is given by

$$\hat{f}(x,y) = \hat{g}(x,y) * u(x,y) = \tilde{f}(x,y) + \tilde{n}(x,y)$$

where $n(x,y)$ is the additive noise and

$$\begin{aligned} g(x,y) &:= \tilde{g}(x,y) + n(x,y) \\ \tilde{f}(x,y) &:= \tilde{g}(x,y) * u(x,y) \\ \tilde{n}(x,y) &:= n(x,y) * u(x,y) \end{aligned}$$

The function $\mathrm{cl}(\cdot)$ is defined as

$$\mathrm{cl}(f) = \begin{cases} 0 & \text{if } f \geq 0 \\ 1 & \text{if } f < 0 \end{cases}$$

The cost function can be written in terms of $\tilde{f}(x,y)$ and $\tilde{n}(x,y)$ as shown below

$$\begin{aligned} J = & \sum_{(x,y)\in D_{sup}} [\tilde{f}^2(x,y) + 2\tilde{f}(x,y)\tilde{n}(x,y) + \tilde{n}^2(x,y)]\mathrm{cl}(\tilde{f}(x,y) + \tilde{n}(x,y)) \\ & + \sum_{(x,y)\in \overline{D_{sup}}} [\tilde{f}^2(x,y) + 2\tilde{f}(x,y)\tilde{n}(x,y) + \tilde{n}^2(x,y) - 2L_B\tilde{f}(x,y) - 2L_B\tilde{n}(x,y) + L_B^2] \end{aligned}$$

Assuming the additive noise is stationary zero-mean and Gaussian, the following expectations are calculated. The term $p_N(n)$ represents the probability density function (pdf) of the noise. Since $n(x,y)$ is zero-mean and Gaussian, $\tilde{n}(x,y)$, which is a filtered version of $n(x,y)$, is also zero-mean and Gaussian with variance

$$\sigma^2 = \sum_{\forall(x_1,y_1)} \sum_{\forall(x_2,y_2)} R_n(x_2 - x_1, y_2 - y_1)u(x_1,y_1)u(x_2,y_2)$$

where $R_n(x,y)$ is the spatial autocorrelation of $n(x,y)$.

$$\begin{aligned} E\{\mathrm{cl}(s+n)\} &= \int_{-\infty}^{\infty} \mathrm{cl}(s+n)p_N(n)dn = \frac{1}{\sqrt{2\pi}\sigma}\int_{-\infty}^{-s} e^{-n^2/2\sigma^2}dn \\ &= 1 - Q\left(\frac{-s}{\sqrt{2}\sigma}\right) \\ E\{n\mathrm{cl}(s+n)\} &= \int_{-\infty}^{\infty} n\mathrm{cl}(s+n)p_N(n)dn \end{aligned}$$

$$
\begin{aligned}
&= \frac{1}{\sqrt{2\pi}\sigma}\int_{-\infty}^{-s} n e^{-n^2/2\sigma^2} dn \\
&= \frac{-\sigma}{\sqrt{2\pi}} e^{-s^2/2\sigma^2} \\
E\{n^2 \mathrm{cl}(s+n)\} &= \int_{-\infty}^{\infty} n^2 \mathrm{cl}(s+n) p_X(n) dn \\
&= \frac{1}{\sqrt{2\pi}\sigma}\int_{-\infty}^{-s} n^2 e^{-n^2/2\sigma^2} dn \\
&= \frac{s\sigma}{\sqrt{2\pi}} e^{-s^2/2\sigma^2} + \sigma^2\left[1 - Q\left(\frac{-s}{\sqrt{2}\sigma}\right)\right]
\end{aligned}
$$

where

$$
Q(s) \triangleq \frac{1}{\sqrt{2\pi}}\int_s^{\infty} e^{-x^2} dx
$$

Using these results the expectation of the cost in the presence of noise at the true inverse PSF $\underline{u}^*$ is evaluated. Here, $\tilde{f}(x,y) = u^*(x,y) * \tilde{g}(x,y) = f(x,y)$, the true image.

$$
\begin{aligned}
E\{J(u^*)\} &= \sum_{(x,y)\in D_{sup}} \left[(f^2(x,y)+\sigma^2)\left(1 - Q\left(\frac{-f(x,y)}{\sqrt{2}\sigma}\right)\right) - \left(\frac{f(x,y)\sigma}{\sqrt{2\pi}}\right) e^{-f^2(x,y)/2\sigma^2}\right] \\
&\quad + \sum_{(x,y)\in \overline{D_{sup}}} \Big[f^2(x,y) + 2f(x,y)E\{\tilde{n}(x,y)\} + E\{\tilde{n}^2(x,y)\} \\
&\quad -2L_B f(x,y) - 2L_B E\{\tilde{n}(x,y)\} + L_B^2\Big] \\
&= \sum_{(x,y)\in D_{sup}} \left[(f^2(x,y)+\sigma^2)\left(1 - Q\left(\frac{-f(x,y)}{\sqrt{2}\sigma}\right)\right) - \sigma\frac{f(x,y)}{\sqrt{2\pi}} e^{-f^2(x,y)/2\sigma^2}\right] \\
&\quad + \sum_{(x,y)\in \overline{D_{sup}}} \sigma^2
\end{aligned}
$$

because $E\{\tilde{n}(x,y)\} = 0$ and $f(x,y)$ is equal to L_B for $(x,y) \in \overline{D_{sup}}$.

For the case that $n(x,y)$ is zero-mean additive white Gaussian noise (AWGN) with variance σ_n^2,

$$
\sigma^2 = \sigma_n^2 \sum_{x=-\infty}^{\infty}\sum_{y=-\infty}^{\infty} [u^*(x_1,y_1)]^2
$$

Therefore, the bias of the cost function due to zero-mean AWGN is given by

$$E\{J(u^*(x,y))\} = \sum_{(x,y)\in D_{sup}} (f^2(x,y)+\sigma^2)\left(1-Q\left(\frac{-f(x,y)}{\sqrt{2}\sigma}\right)\right) - \sum_{(x,y)\in D_{sup}} \sigma\frac{f(x,y)}{\sqrt{2\pi}}\epsilon^{-f^2(x,y)/2\sigma^2} + \sigma^2 \parallel \overline{D_{sup}} \parallel$$

where $\parallel \overline{D_{sup}} \parallel$ represents the number of elements in $\overline{D_{sup}}$.

C.2 Effect of Noise on Support Constraint Cost Function

The proposed cost function is the sum of a non-quadratic term representing the non-negativity constraint, and a perfectly quadratic term representing the support constraint. Ideally, both terms should both have a global minimum at the same location. That is, their costs should be zero at the true solution. If only the cost corresponding support constraint is considered, the effect of noise on the global minimum is straightforward to calculate. As discussed in section 4.2.2, if the image is highly positive, noise has little effect on it at moderate levels, thus, in such situations, the effect of noise on the global minimum of the support constraint cost function alone can lead to valuable insight into the effect of noise on the overall solution.

The cost function for the support constraint can be represented using lexicographically ordered matrices as

$$\begin{aligned} J_2 &= \sum_{(x,y)\in\overline{D_{sup}}} (\hat{f}(x,y)-L_B)^2 \\ &= [\underline{Gu_k}-\underline{L}]^T S[\underline{Gu_k}-\underline{L}] \end{aligned}$$

where $N_{xu} \times N_{yu}$ is the dimension of the equalizer, $N_{xg} \times N_{yg}$) is the size of the blurred image, and $N_{xf} \times N_{yf}$ is the size of the restored image. Because $\hat{f}(x,y) =$

$u(x,y) * g(x,y)$.

$$\begin{aligned} N_{xf} &= N_{xg} + N_{xu} - 1 \\ N_{yf} &= N_{yg} + N_{yu} - 1 \end{aligned}$$

The matrices are defined as

$$\underline{u_k} = \begin{bmatrix} u(1,1) \\ u(1,2) \\ \vdots \\ u(N_{xu}, N_{yu}) \end{bmatrix} \quad \underline{G} = \begin{bmatrix} g(1,1) & g(1,0) & \cdots & g(-N_{xu}+2, -N_{yu}+2) \\ g(1,2) & g(1,1) & & g(-N_{xu}+2, -N_{yu}+3) \\ \vdots & \vdots & & \vdots \\ g(N_{xf}, N_{yf}) & g(N_{xf}, N_{yf}-1) & \cdots & g(N_{xg}, N_{yg}) \end{bmatrix}$$

and the elements of $\underline{L}$ are given by

$$[\underline{L}]_{y+(x-1)N_{yf}} = \begin{cases} L_B & \text{if } (x,y) \in \overline{D_{sup}} \\ 0 & \text{otherwise} \end{cases}$$

for $1 \leq x \leq N_{xf}$ and $1 \leq y \leq N_{yf}$. $\underline{S}$ is a diagonal matrix with the diagonal entries being 1 or 0, such that

$$[\underline{S}]_{y+(x-1)N_{yf}, y+(x-1)N_{yf}} = \begin{cases} 1 & \text{if } (x,y) \in \overline{D_{sup}} \\ 0 & \text{if } (x,y) \in D_{sup} \end{cases}$$

for $1 \leq x \leq N_{xf}$ and $1 \leq y \leq N_{yf}$.

The cost function may be reformulated as

$$J = [\underline{\hat{G}} \underline{u_k} - \underline{L}]^T \underline{S} [\underline{\hat{G}} \underline{u_k} - \underline{L}]$$

where $\underline{\hat{G}} = \underline{SG}$. The global minimum of this cost is well known, and can be represented in terms of the singular values of $\underline{\hat{G}}$ as shown below.

$$u^* = \sum_{m,n} \frac{\underline{v}_{m,n}^T \underline{L} \underline{w}_{m,n}}{\lambda_{m,n}} \qquad (C.2)$$

where $\{\lambda_{m,n}\}$ are the singular values of $\underline{\hat{G}}$ and $\{\underline{v}_{m,n}\}$, $\{\underline{w}_{m,n}\}$ are the associated eigenvectors such that

$$\begin{aligned}(\underline{\hat{G}}^T\underline{\hat{G}})\underline{w}_{m,n} &= \lambda^2_{m,n}\underline{w}_{m,n}\\ (\underline{\hat{G}}\underline{\hat{G}}^T)\underline{v}_{m,n} &= \lambda^2_{m,n}\underline{v}_{m,n}\end{aligned}$$

When the blurred image is perturbed by noise, $\underline{\hat{G}}$ is replaced with $\underline{\tilde{G}}$, such that

$$\underline{\tilde{G}} = \underline{\hat{G}} + \underline{\hat{N}}$$

where $\underline{\hat{N}} = \underline{SN}$, and

$$\underline{N} = \begin{bmatrix} n(1,1) & n(1,0) & \cdots & n(-N_{xu}+2,-N_{yu}+2)\\ n(1,2) & n(1,1) & & n(-N_{xu}+2,-N_{yu}+3)\\ \vdots & \vdots & & \vdots\\ n(N_{xf},N_{yf}) & n(N_{xf},N_{yf}-1) & \cdots & n(N_{xg},N_{yg})\end{bmatrix}$$

Therefore,

$$\begin{aligned}E\{\underline{\tilde{G}}^T\underline{\tilde{G}}\} &= E\{\underline{\hat{G}}^T\underline{\hat{G}} + \underline{\hat{N}}^T\underline{\hat{G}} + \underline{\hat{N}}\underline{\hat{G}}^T + \underline{\hat{N}}^T\underline{\hat{N}}\}\\ &= \underline{\hat{G}}^T\underline{\hat{G}} + E\{N^TSN\}\end{aligned}$$

For zero-mean white Gaussian noise $n(x,y)$ of variance σ_n^2,

$$E\{\underline{\tilde{G}}^T\underline{\tilde{G}}\} = \hat{G}^T\hat{G} + \parallel D_{sup} \parallel \sigma_n^2 I_{N_{xu}N_{yu},N_{xu}N_{yu}}$$

where $I_{N_{xu}N_{yu},N_{xu}N_{yu}}$ is the $N_{xu}N_{yu} \times N_{xu}N_{yu}$ identity matrix.

The eigenvectors of $E\{\underline{\tilde{G}}^T\underline{\tilde{G}}\}$ are the same as for $\underline{\hat{G}}^T\underline{\hat{G}}$, but the eigenvalues are equal to $\lambda^2_{m,n} + parallel D_{sup} \parallel \sigma_n^2$. Therefore, on average, the noise has the effect of perturbing the eigenvalues of $E\{\underline{\tilde{G}}^T\underline{\tilde{G}}\}$ by a quantity proportional to σ_n^2. The smaller the singular value $\lambda_{m,n}$ the greater the relative perturbation, and the greater the effect on the solution of equation C.2.

In general, to successfully identify the inverse blur, the singular values of $\underline{G}$ must be large compared to σ_n.

References

[1] A. K. Katsaggelos, ed., *Digital Image Restoration*. New York: Springer-Verlag, 1991.

[2] H. C. Andrews and B. R. Hunt, *Digital Image Restoration*. Prentice-Hall, Inc., New Jersey, 1977.

[3] M. E. Zervakis, *Nonlinear Image Restoration Techniques*. Ph.D. Thesis, University of Toronto, 1990.

[4] J. P. Muller, ed., *Digital Image Processing in Remote Sensing*, pp. 226-269, Philadelphia: Taylor & Francis, 1988.

[5] R. H. T. Bates, "Astronomical speckle imaging," *Phys. Rep.*, vol. 90(4), pp. 203-97, Oct. 1982.

[6] T. J. Schulz, "Multiframe blind deconvolution of astronomical images," *J. Opt. Soc. Am. A*, vol. 10(5), pp. 1064-1073, May 1993.

[7] M. J. B. Crowther and M. C. Fernandez, "Imaging in videoconferencing now: telemedicine in Somalia," *Advanced Imaging*, pp. 28-31, Oct. 1993.

[8] A. G. Qureshi and H. T. Mouftah, "Partially-blind image restoration using constrained Kalman filtering," *Proc. IEEE Int. Conf. Acoustics, Speech, Signal Processing*, pp. 3713-3716, 1991.

[9] V. Krishnamurthi, Y. H. Lui, T. J. Holmes, B. Roysam and J. N. Turner, "Blind deconvolution of 2D and 3D fluorescent micrographs," *Biomedical Image*

Processing and Three-Dimensional Microscopy, Proc. SPIE, vol. 1660, pp. 95-102, 1992.

[10] P. Nisenson and R. Barakat, "Partial atmospheric correction with adaptive optics," *J. Opt. Soc. Am. A*, vol. 4, pp. 2249-2253, 1991.

[11] M. C. Roggemann, "Limited degree-of-freedom adaptive optics and image reconstruction," *Applied Optics*, vol. 30, pp. 4227-4233, 1991.

[12] K. Faulkner, C. J. Kotre and M. Louka, "Veiling glare deconvolution of images produced by x-ray image intensifiers," *Third Int. Conf. on Image Proc. and Its Applications*, pp. 669-673, July 1989.

[13] M. Cannon, "Blind deconvolution of spatially invariant image blurs with phase," *IEEE Trans. Acoust. , Speech, Signal Process.* , vol. 24(1), pp. 58-63, Feb. 1976.

[14] M. M. Chang, A. M. Tekalp and A. T. Erdem, "Blur identification using the bispectrum," *IEEE Trans. Signal Processing*, vol. 39(10), pp. 2323-2325, Oct. 1991.

[15] R. Fabian and D. Malah, "Robust identification of motion and out-of-focus blur parameters from blurred and noisy images," *CVGIP: Graphical Models and Image Processing*, vol. 53(5), pp. 403-412, Sept. 1991.

[16] B. Chalmond, "PSF estimation for image deblurring," *CVGIP: Graphical Models and Image Processing*, vol. 53(4), pp. 364-372, July 1991.

[17] G. R. Ayers and J. C. Dainty, "Iterative blind deconvolution method and its applications," *Optics Letters*, vol. 13(7), pp. 547-549, July 1988.

[18] B. L. K. Davey, R. G. Lane and R. H. T. Bates, "Blind deconvolution of noisy complex-valued image," *Optics Communications*, vol. 69(5,6), pp. 353-356, Jan. 1989.

[19] J. H. Seldin and J. R. Fienup, "Iterative blind deconvolution algorithm applied to phase retrieval," *J. Opt. Soc. Am. A*, vol. 7(3), pp. 428-433, Mar. 1990.

[20] N. Miura and N. Baba, "Extended-object reconstruction with sequential use of the iterative blind deconvolution method," *Optics Communications*, vol. 89, pp. 375-379, 1992.

[21] N. Miura, N. Baba, S. Isobe, M. Noguchi and Y. Norimoto, "Binary star reconstruction with use of the blind deconvolution method," *Journal of Modern Optics*, vol. 39(5), pp. 1137-1146, May 1992.

[22] F. Tsumuraya, N. Miura and N. Baba, "Iterative blind deconvolution method using Lucy's algorithm," *Astron. Astrophys.*, vol. 282(2), pp. 699-708, Feb. 1994.

[23] N. Miura, K. Ohsawa and N. Baba, "Single-frame blind deconvolution by means of frame segmentation," *Optics Letters*, vol. 19(10), pp. 695-697, May 1994.

[24] R. G. Lane, "Blind deconvolution of speckle images," *J. Opt. Soc. Am. A.*, vol. 9(9), pp. 1508-1514, Sept. 1992.

[25] B. C. McCallum, "Blind deconvolution by simulated annealing," *Optics Communications*, vol. 75(2), pp. 101-105, Feb. 1990.

[26] R. L. Lagendijk, A. M. Tekalp and J. Biemond, "Maximum likelihood image and blur identification: a unifying approach," *Optical Engineering*, vol. 29(5), pp. 422-435, May 1990.

[27] R. L. Lagendijk, J. Biemond and D. E. Boekee, "Identification and restoration of noisy blurred images using the expectation-maximization algorithm," *IEEE Trans. Acoust. , Speech, Signal Process.* , vol. 38(7), July 1990.

[28] S. J. Reeves and R. M. Mersereau, "Blur identification by the method of generalized cross-validation," *IEEE Trans. Image Processing*, vol. 1(3), pp. 301-311, July 1992.

[29] A. K. Jain, "Advances in mathematical models for image processing," *Proc. IEEE*, vol. 69(5), pp. 502-528, May 1981.

[30] H. Kaufman and A. M. Tekalp, "Survey of estimation techniques in image restoration," *IEEE Control Systems*, pp. 16-24, Jan. 1991.

[31] R. A. Wiggins, "Minimum entropy deconvolution," *Geoexploration*, vol. 16, pp. 21-35, 1978.

[32] G. Jacovitti and A. Neri, "A Bayesian approach to 2D non minimum phase AR identification," *Fifth AASP Workshop on Spectrum Estimation and Modelling*, pp. 79-83, 1990.

[33] R. G. Lane and R. H. T. Bates, "Automatic multidimensional deconvolution," *J. Opt. Soc. Am. A*, vol. 4(1), pp. 180-188, Jan. 1987.

[34] D. C. Ghiglia, L. A. Romero and G. A. Mastin, "Systematic approach to two-dimensional blind deconvolution by zero-sheet separation," *J. Opt. Soc. Am. A*, vol. 10(5), pp. 1024-1036, May 1993.

[35] R. K. Ward and E. Lam, "Semi-blind restoration from differently blurred versions of an image," *Proc. IEEE Int. Conf. Acoustics, Speech, Signal Processing*, pp. 2949-2952, 1991.

[36] A. P. Petropulu and C. L. Nikias, "Blind deconvolution using signal reconstruction from partial higher order cepstral information," *IEEE Trans. Signal Processing*, vol. 41(6), pp. 2088-2095, June 1993.

[37] R. M. Mersereau and R. W. Schafer, "Some techniques for digital deconvolution of positive constrained multi-dimensional sequences," *Proc. 1978 European Conf. Ciruit Theory and Design*, pp. 404-409, Sept. 1978.

[38] R. M. Mersereau and R. W. Schafer, "Comparative study of iterative deconvolution algorithms," *Proc. IEEE Int. Conf. Acoustics, Speech, Signal Processing*, pp. 192-195, Apr. 1978.

[39] R. W. Schafer, R. M. Mersereau and M. A. Richards, "Constrained iterative signal restoration algorithms," *Proc. IEEE*, vol. 69, pp. 432-450, Apr. 1981.

[40] J. Biemond, R. L. Lagendijk and R. M. Mersereau, "Iterative methods for image deblurring," *Proc. IEEE*, vol. 78(5), pp. 856-883, May 1990.

[41] D. C. Youla, H. Webb, "Image restoration by method of convex projections: part 1 - theory," *IEEE Trans. on Medical Imaging*, vol. MI-1, no. 2, pp. 81-94, Oct. 1982.

[42] D. C. Youla, H. Webb, "Image restoration by method of convex projections: part 2 -applications and numerical results," *IEEE Trans. on Medical Imaging*, vol. MI-1, no. 2, pp. 95-101, Oct. 1982.

[43] S. Vembu, S. Verdù, R. A. Kennedy and W. Sethares, "Convex cost function in blind equalization," *IEEE Trans. Signal Processing*, vol. 42(8), pp. 1952-1960, Aug. 1994.

[44] J. B. Hiriart-Urruty and C. Lemarécal, *Convex Analysis and Minimization Algorithms I.* Springer-Verlag, New York:1993.

[45] C. T. Chen, *Linear System Theory and Design.* pp. 413, Harcourt Brace Jovanovich College Publishers, Toronto: 1984.

[46] S. M. Kay, *Modern Spectral Estimation*, pp. 185-190, Prentice Hall, Toronto:1988.

[47] E. Polak, *Computational Methods in Optimization.* Academic Press, New York: 1971.

[48] R. Fletcher, *Practical Methods of Optimization, vol. 1: Unconstrained Optimization*, Wiley, Chichester:1980.

[49] W. H. Press, S. A. Toukolsky, W. T. Vetterling and B. P. Flannery, *Numerical Recipes in C, The Art of Scientific Computing*, 2nd ed., Cambridge University Press, New York: 1992.

[50] D. A. H. Jacobs,ed., *The State of the Art in Numerical Analysis.* , Academic Press, London: 1977.

[51] R. Marucii, R. M. Mersereau and R. W. Schafer, "Constrained iterative deconvolution using a conjugate gradient algorithm," *Proc. IEEE Int. Conf. Acoustics, Speech, Signal Processing*, pp. 1845-1848, 1982.

[52] R. Prost and R. Goutte, "Discrete constrained iterative deconvolution with optimized rate of convergence," *Signal Processing*, vol. 7, pp. 209-230, Dec. 1984.

[53] T. K. Sarkar, F. I. Tseng, S. A. Dianat and B. Z. Hollmann, "Deconvolution by the conjugate gradient method," *Proc. IEEE Int. Conf. Acoustics, Speech, Signal Processing*, pp. 445-488, Mar. 1985.

[54] R. L. Lagendijk, R. M. Mersereau and J. Biemond, "On increasing the convergence rate of regularized iterative image restoration algorithms," *Proc. IEEE Int. Conf. Acoustics, Speech, Signal Processing*, pp. 1183-1186, 1987.

[55] H. J. Trussell, "Convergence criteria for iterative restoration methods," *IEEE Trans. Acoust. , Speech, Signal Process.* , vol. 31(1), pp. 201-212, Feb. 1983.

[56] B. W. Dickinson, *Systems Analysis, Design and Computation.* pp. 234-279, Prentice Hall Inc. , Englewood Cliffs, New Jersey: 1991.

[57] M. Z. Nashed, "Aspects of generalized inverses in analysis and regularization," *Generalized Inverses and Applications*, M. Z. Nashed, ed., Academic Press, New York: 1976.

[58] N. B. Karayiannis and A. N. Venetsanopoulos, "Regularization theory in image restoration: the regularizing operator approach," *Optical Engineering*, vol. 28(7), pp 761-780, July 1989.

[59] H. J. Trussell and M. R. Civanlar, "The feasible solution in signal restoration," *IEEE Trans. Acoust., Speech, and Signal Processing*, vol. 32(2), pp. 201-212, April 1984.

[60] B. J. Sullivan, A. K. Katsaggelos, "New termination rule for linear iterative image restoration algorithms," *Optical Engineering*, vol. 29(5), pp. 471- 477, May 1990.

[61] B. J. Sullivan and H. C. Chang, "A generalized landweber iteration for ill-conditioned signal restoration," *Proc. IEEE Int. Conf. Acoustics, Speech, Signal Processing*, pp. 1729-1732, 1991.

[62] S. J. Reeves and K. M. Perry "A practical stopping rule for iterative image restoration," *Image Processing Algorithms and Techniques III*, Proc. SPIE, vol. 1657, pp. 192-200, 1992.

[63] G. H. Golub, M. Heath and G. Wahba, "Generalized cross-validation as a method for choosing a good ridge parameter," *Technometrics*, vol. 21, no. 2, pp. 215-223, May 1979.

[64] S. J. Reeves and R. M. Mersereau, "Optimal constraint parameter estimation for constrained image restoration," *Visual Communications and Image Processing '90*, Proc. SPIE, vol. 1360, pp. 1372-1380, 1990.

[65] S. J. Reeves and M. Mersereau, "Automatic Assessment of constraint sets in image restoration," *IEEE Trans. Image Processing*, vol. 1(1), pp. 119-123, Jan. 1992

END

19-04-96

FIN